**Electronic Supplementary Information**

**Robust covalent pyrazine anchors forming highly conductive and polarity-tunable molecular junctions with carbon electrodes**

Yudi Wang,[a] Haoyang Pan,[ab] Dongying Lin,[a] Shi Li,[a] Yongfeng Wang,[a] Stefano Sanvito[c] and Shimin Hou[*ab]

a Key Laboratory for the Physics and Chemistry of Nanodevices, School of Electronics, Peking University, Beijing 100871, China. Email: smhou@pku.edu.cn

2 Centre for Nanoscale Science and Technology, Academy for Advanced Interdisciplinary Studies, Peking University, Beijing 100871, China

3 School of Physics, AMBER and CRANN Institute, Trinity College, Dublin 2, Ireland

**Table of contents**

**Section 1:** Phonon spectrum calculations on molecular junctions constructed with pyrazine anchors and carbon electrodes
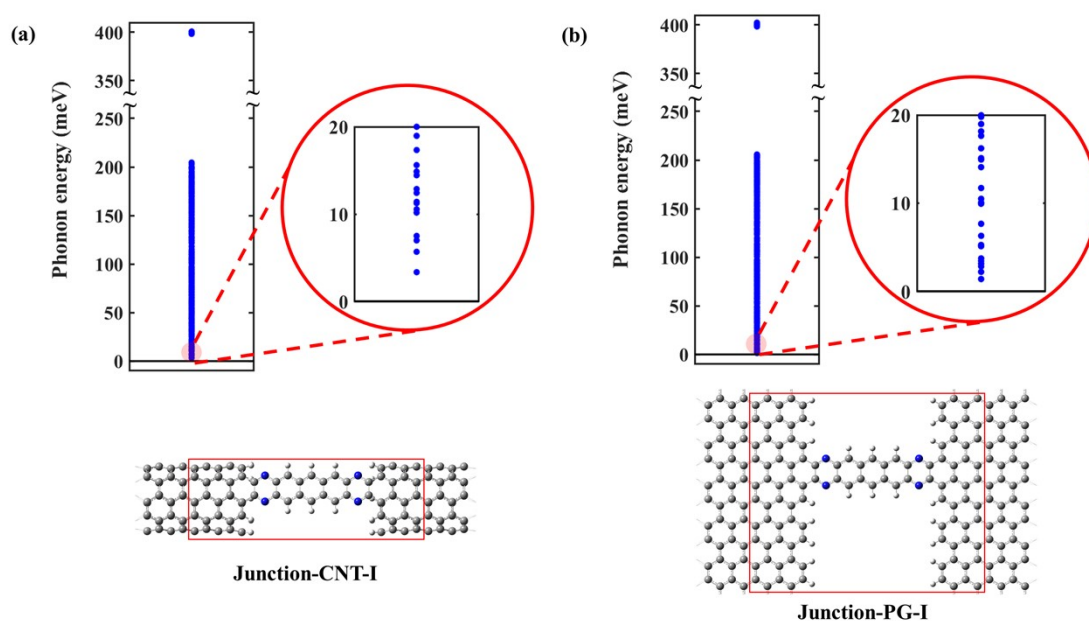


**Fig. S1** Vibrational frequencies (the upper panel) calculated for Junction-CNT-I (a) and Junction-PG-I (b) with the dynamic regions denoted by the red boxes (the bottom panel).

The phonon spectra of the junctions are computed by using the frozen phonon method,[1] in which the force constant matrix is calculated by displacing each atom in the dynamic region along the coordinate directions with a displacement of ±0.02 Å and by calculating the resulting forces acting on the atoms.

The phonon spectrum of Junction-CNT-I is shown in Fig. S1a. As we can see, there are no imaginary frequencies in the low-frequency region, indicating that the junction structure is at least a local minimum. The much higher frequencies around 400 meV are assigned to the stretching modes of the C-H bonds due to the much smaller mass of the hydrogen atoms. Similar results are also obtained for the phonon spectrum of Junction-PG-I (Fig. S1b), indicating that the junction structures constructed via the pyrazine anchors are dynamically stable with both graphene and SWCNT electrodes.

**Section 2:** Molecular dynamics simulations on molecular junctions constructed with pyrazine anchors and carbon electrodes
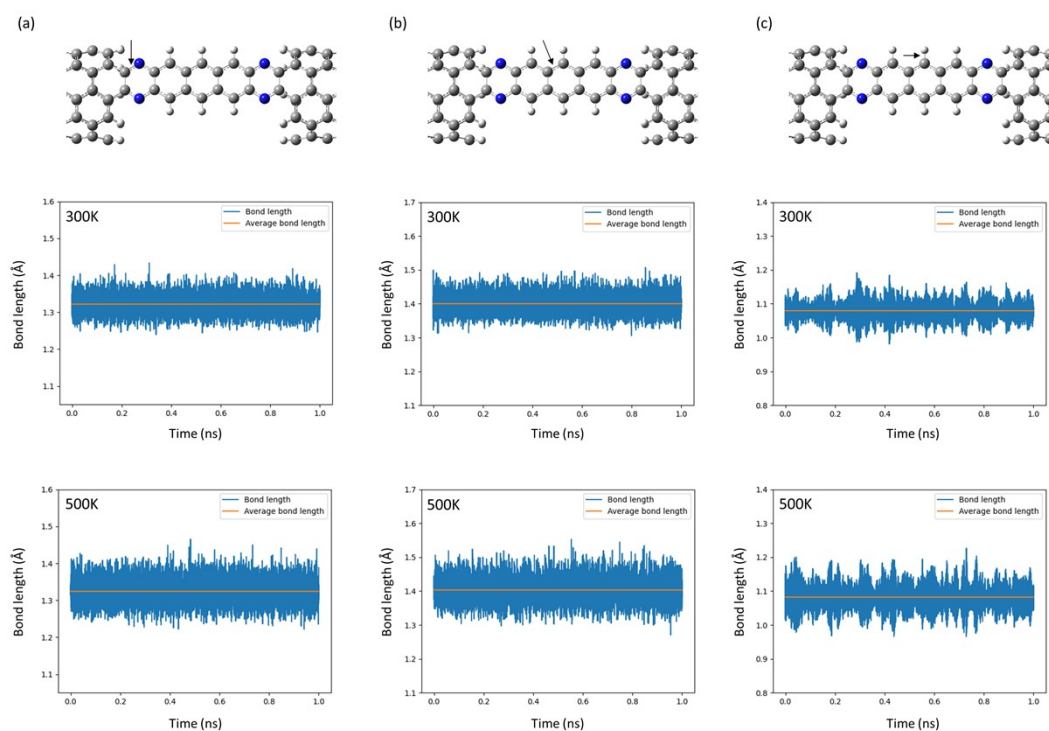


**Fig. S2** Variation in the C-N (a), C-C (b), and C-H (c) bond lengths denoted by black arrows (the upper panel) in Junction-CNT-I obtained from MD simulations performed at 300 K (the middle panel) and 500 K (the bottom panel).

**Table S1** Average bond lengths, standard deviations, and maximum deviations of the C-N, C-C, and C-H bonds in Junction-CNT-I shown in Fig. S2 at 300 K and 500 K.

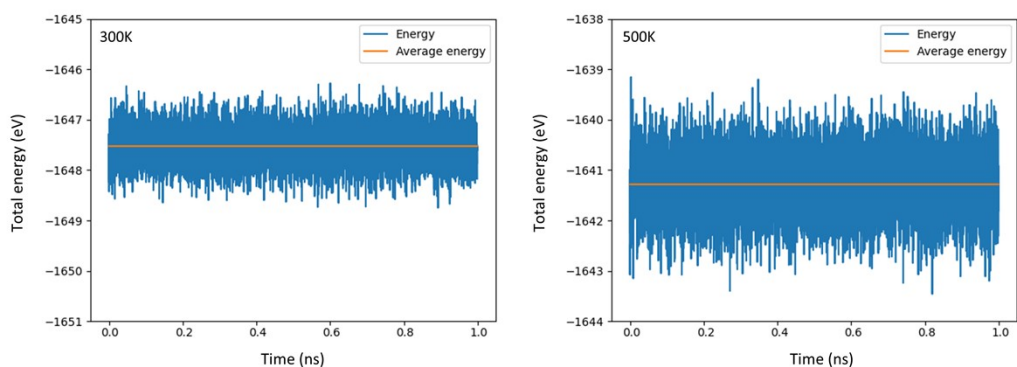| Bond type | C-N | | C-C | | C-H | |
|---|---|---|---|---|---|---|
| Temperature (K) | 300 | 500 | 300 | 500 | 300 | 500 |
| Average bond length (Å) | 1.32 | 1.32 | 1.40 | 1.40 | 1.08 | 1.08 |
| Standard deviation (Å) | 0.02 | 0.03 | 0.03 | 0.03 | 0.03 | 0.04 |
| Maximum deviation (Å) | 0.11 | 0.14 | 0.11 | 0.15 | 0.11 | 0.14 |
| Bond length calculated using DFT (Å) | 1.32 | | 1.41 | | 1.10 | |

**Fig. S3** Variation in the total energy of Junction-CNT-I obtained from MD simulations performed at 300 K (the left panel) and 500 K (the right panel).

**Table S2** Average energies, standard deviations, and maximum deviations of the total energies of Junction-CNT-I shown in Fig. S3 at 300 K and 500 K.

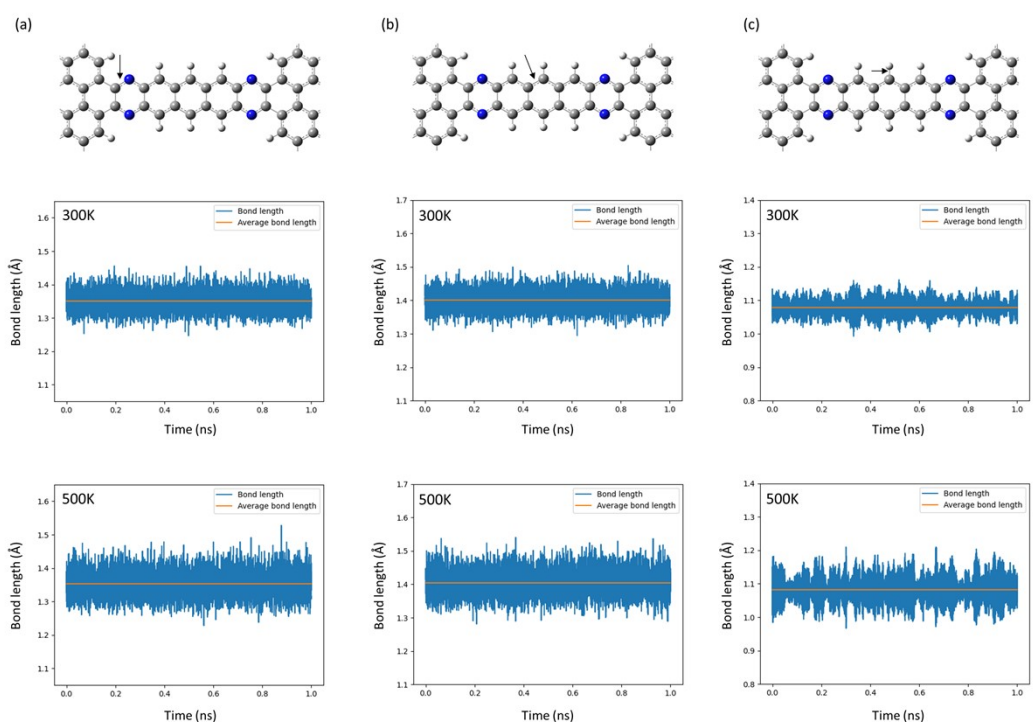| Temperature (K) | 300 | 500 |
|---|---|---|
| Average energy (eV) | -1647.53 | -1641.28 |
| Standard deviation (eV) | 0.35 | 0.58 |
| Maximum deviation (eV) | 1.25 | 2.18 |



**Fig. S4** Variation in the C-N (a), C-C (b), and C-H (c) bond lengths denoted by black arrows (the upper panel) in Junction-PG-I obtained from MD simulations performed at 300 K (the middle panel) and 500 K (the bottom panel).

**Table S3** Average bond lengths, standard deviations, and maximum deviations of the C-N, C-C, and C-H bonds in Junction-PG-I shown in Fig. S4 at 300 K and 500 K.

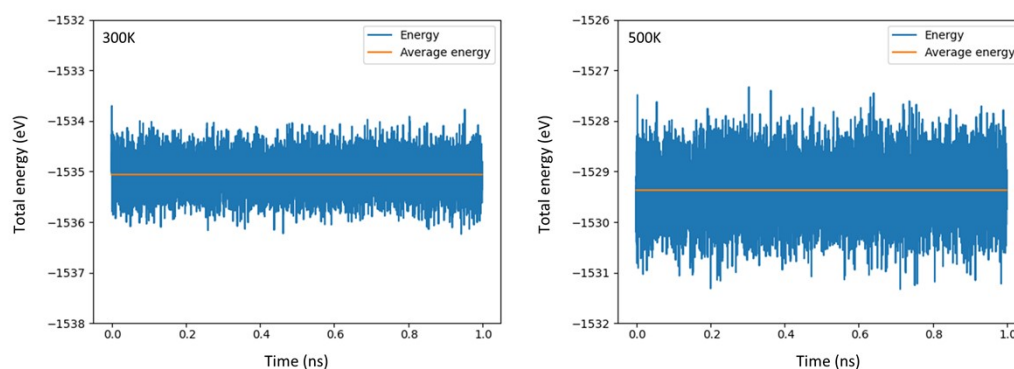| Bond type | C-N | | C-C | | C-H | |
|---|---|---|---|---|---|---|
| Temperature (K) | 300 | 500 | 300 | 500 | 300 | 500 |
| Average bond length (Å) | 1.35 | 1.35 | 1.40 | 1.40 | 1.08 | 1.08 |
| Standard deviation (Å) | 0.03 | 0.03 | 0.03 | 0.03 | 0.02 | 0.04 |
| Maximum deviation (Å) | 0.11 | 0.17 | 0.11 | 0.14 | 0.09 | 0.13 |
| Bond length calculated using DFT (Å) | 1.33 | | 1.41 | | 1.09 | |



**Fig. S5** Variation in the total energy of Junction-PG-I obtained from MD simulations performed at 300 K (the left panel) and 500 K (the right panel).

**Table S4** Average energies, standard deviations, and maximum deviations of the total energies of Junction-PG-I shown in Fig. S5 at 300 K and 500 K.

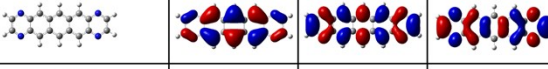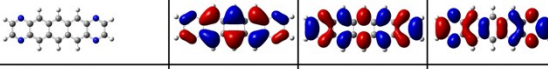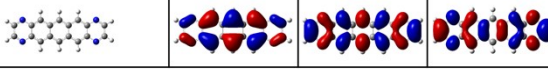| Temperature (K) | 300 | 500 |
|---|---|---|
| Average energy (eV) | -1535.06 | -1529.37 |
| Standard deviation (eV) | 0.33 | 0.55 |
| Maximum deviation (eV) | 1.36 | 2.04 |

Molecular dynamics (MD) simulations are performed with the xtb program,[2] where forces and energies are calculated using the GFN-FF force field.[3] The Newtonian equations of motion of the atoms in the junction are then integrated via the velocity Verlet algorithm with a time step of 1.0 fs. A Berendsen thermostat maintains the average temperature at either 300 K or 500 K. During the MD the configurations are recorded every 100 fs.

At the selected temperatures we run MD calculations for Junction-CNT-I for 1ns and record 10000 configurations. Junction-CNT-I is very stable at room temperature (300 K) and even when the temperature is increased to 500 K, we do not observe the occurrence of any bond cleavage. For the typical C-N, C-C and C-H bonds in the central molecule, the average bond lengths, standard deviations, and maximum deviations are listed in Table S1. As we can see, the average bond lengths of the C-N, C-C and C-H bonds are respectively calculated to be 1.32, 1.40 and 1.08 Å, which are in excellent agreement with the DFT optimized values of 1.32, 1.41 and 1.10 Å. This further confirms the reliability of the GFN-FF force field for this material set. At room temperature, the

maximum deviations for these three bonds are 0.11 Å; when the temperature increases to 500 K, the maximum deviations are 0.14~0.15 Å, illustrating the robustness of these covalent bonds. Similar results are also obtained from MD simulations for Junction-PG-I, for which we also record 10000 configurations along 1 ns and do not find any bond cleavage even at 500 K. As shown in Table S3, the average bond lengths of the C-N, C-C and C-H bonds are respectively calculated to be 1.35, 1.40 and 1.08 Å, which are also in excellent agreement with the DFT optimized values of 1.33, 1.41 and 1.09 Å. Considering the small standard deviations of both bond lengths and total energies (Tables S1-S4), we can conclude that the covalent pyrazine anchors are advantageous for forming stable and robust molecular junctions with carbon electrodes.

# Section 3: Effects of approximate density functionals on the electronic structures of isolated molecules and junctions

(a)

| Molecule M1 | Frontier molecular orbitals | HOMO | LUMO | LUMO+1 |
|---|---|---|---|---|
| PBE | Energy (eV) | -5.10 | -4.02 | -3.12 |
| TPSS | Energy (eV) | -5.01 | -3.88 | -2.96 |
| HSE06 | Energy (eV) | -5.37 | -3.65 | -2.56 |

(b)
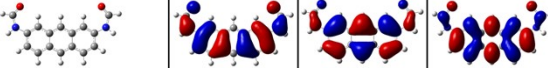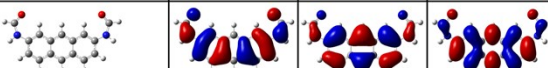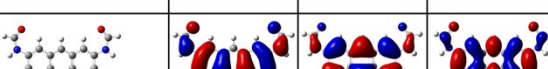
| Molecule M3 | Frontier molecular orbitals | HOMO-1 | HOMO | LUMO |
|---|---|---|---|---|
| PBE | Energy (eV) | -5.69 | -4.95 | -2.78 |
| TPSS | Energy (eV) | -5.64 | -4.88 | -2.62 |
| HSE06 | Energy (eV) | -6.17 | -5.32 | -2.32 |

**Fig. S6** Frontier molecular orbitals of the isolated molecules M1 (a) and M3 (b), calculated using the Gaussian16 package at the PBE/6-311+G(d,p), TPSS/6-311+G(d,p), and HSE06/6-311+G(d,p) levels.[4]

It is well-known that GGA functionals, such as PBE, do not describe the derivative discontinuity of the DFT potential and they are not self-interaction free.[5,6] This drawback may artificially push the occupied molecular orbitals to higher energies and reduce the HOMO-LUMO gap. In contrast, the HSE06 hybrid functional incorporates short-range Hartree-Fock exchange, partially correcting the self-interaction error, so that it provides an improved description of a range of materials and properties.[7-10] First, we calculate the frontier molecular orbitals (FMOs) of the isolated M1 and M3 molecules using the PBE GGA functional, the TPSS meta-generalized gradient approximation (meta-GGA) functional,[11] and the HSE06 hybrid functional. As we can see, the shapes of these FMOs calculated at these three different approximate functionals are completely the same (Fig. S6). The energy levels of these FMOs calculated using the TPSS meta-GGA functional are slightly different from those with the PBE GGA functional. As expected, HSE06 shifts downward the HOMO and also enlarges the HOMO-LUMO gap. For example, the M1 HOMO is shifted from -5.10 eV to -5.37 eV while the M1 LUMO is shifted from -4.02 eV to -3.65 eV, so that the M1 HOMO-LUMO gap is increased from 1.08 eV to 1.72 eV.

Since the coupling of the molecule to the electrodes results in an energy shift and level broadening,[12] next we move to investigate the effects of different approximate functionals on the

projected density of states (PDOS) of the central molecule M1 attached to the graphene and (5,5) armchair SWCNT electrodes. This is realized by using the Vienna Ab initio Simulation Package (VASP) with both the PBE GGA and HSE06 functionals.[13-15] Taking Junction-PG-I as an example, we use a kinetic-energy cutoff of 400 eV and the convergence criteria for the electronic step is $10^{-4}$ eV. The Brillouin zone is sampled by a set of 1×5×3 k-points. We also use the Gaussian smearing method and a width of 0.05 eV is adopted. As shown in Fig. S7, three prominent peaks appear around $E_F$ in the PDOS plots for the central molecule M1 in Junction-PG-I. More importantly, for both the PBE and HSE06 functionals the PDOS peaks associated to the M1 LUMO is much closer to $E_F$ as compared to the HOMO-dominated ones. The assignment of these PDOS peaks in Junction-PG-I can be realized by comparison with those of the isolated M1 molecule (Fig. S8), for which the increasing proportion of the PDOS of N atoms is observed for HOMO, LUMO and LUMO+1. Similar results are also obtained for the PDOS plot of the central molecule M1 in Junction-CNT-I (Fig. S9), indicating that the PBE GGA functional is rather adequate for the low-bias transport calculations of these specific molecular junctions with carbon electrodes. Note that in Junction-CNT-I only a single k-point (the Γ-point) is employed.
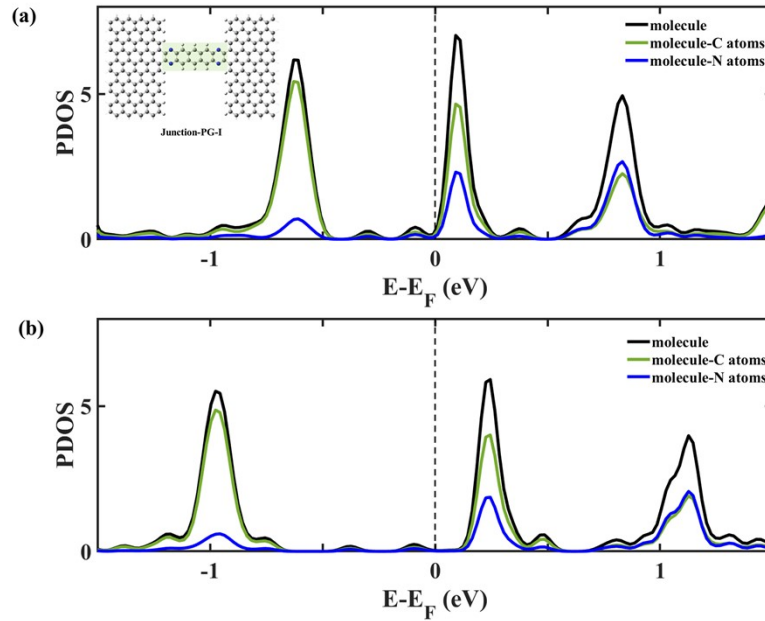


**Fig. S7** Comparison of the PDOS of the central molecule (green square in the inset of the upper panel) in Junction-PG-I (black lines), carbon atoms (green lines) and nitrogen atoms (blue lines) in the central molecule between the PBE (a) and HSE06 (b) functionals.

**Fig. S8** PDOS of the isolated M1 molecule (black), carbon atoms (green) and nitrogen atoms (blue) in M1 calculated using VASP with the PBE GGA functional.



**Fig. S9** Comparison of the PDOS of the central molecule (green ellipse in the inset of the upper panel) in Junction-CNT-I (black lines), carbon atoms (green lines) and nitrogen atoms (blue lines) in the central molecule between the PBE (a) and HSE06 (b) functionals.
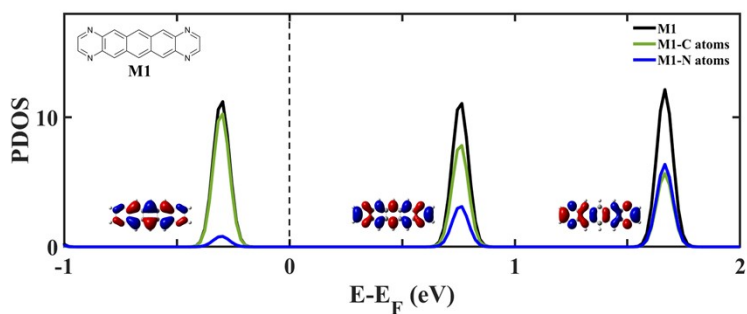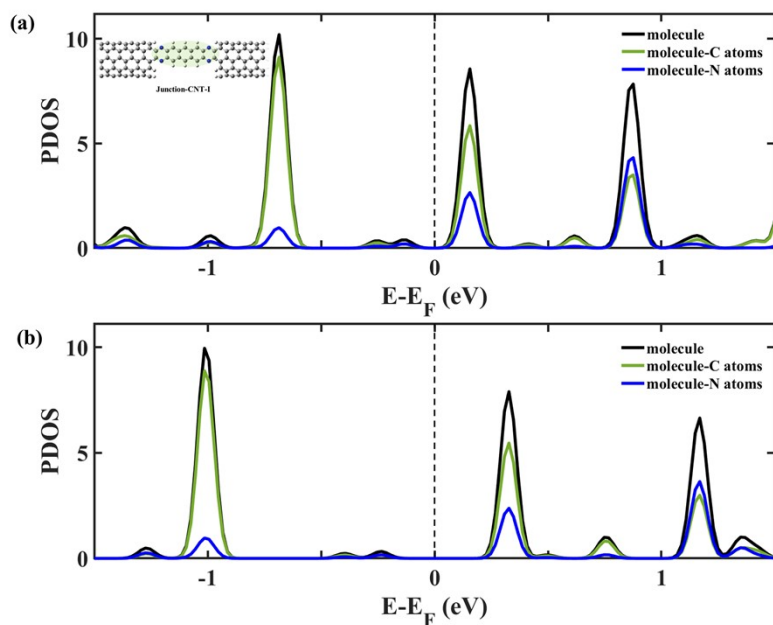
**Section 4:** Reliability of our junction models to describe single-molecule transport properties
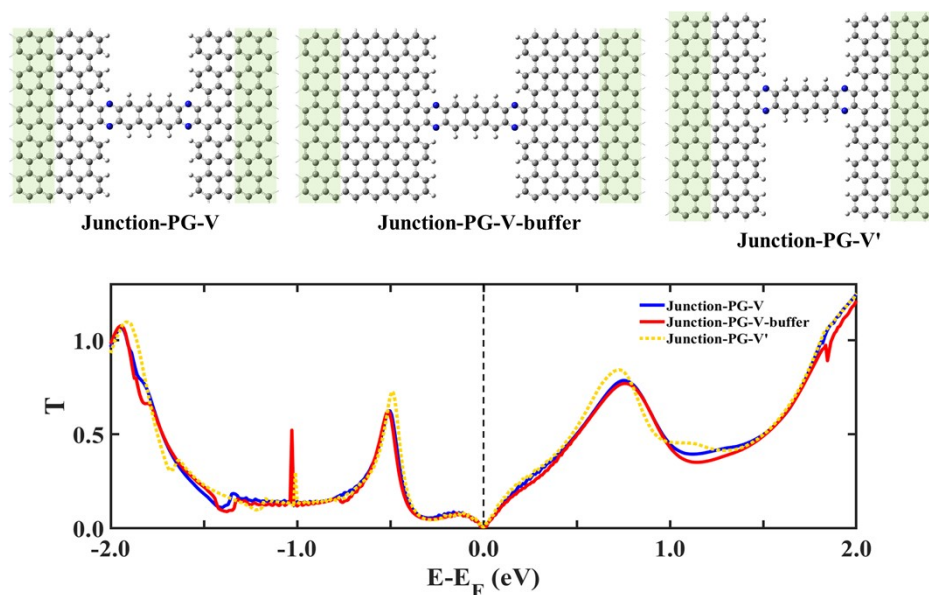


**Fig. S10** Optimized atomic structures of Junction-PG-V, Junction-PG-V-buffer with longer buffer regions, and Junction-PG-V' with larger graphene electrodes, together with their corresponding equilibrium transmission spectra. The green squares denote the principal layers of the graphene electrodes.
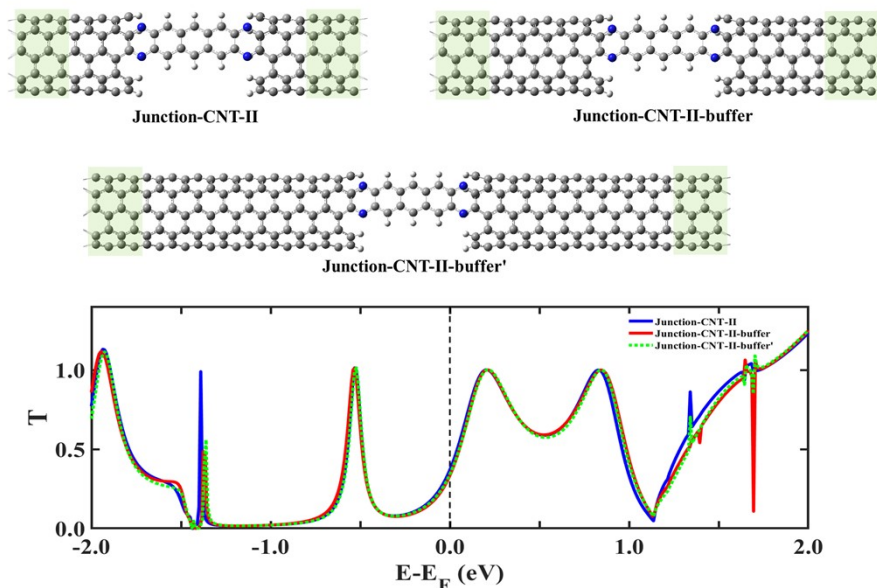


**Fig. S11** Optimized atomic structures of Junction-CNT-II, Junction-CNT-II-buffer and Junction-CNT-II-buffer' with longer buffer regions together with their corresponding equilibrium transmission spectra. The green squares denote the principal layers of the SWCNT electrodes.

Some parts of the electrodes should be included in the junction models for simulating single-molecule transport with the NEGF+DFT approach. These parts of the electrodes should be large enough to guarantee that both the density matrix and the Hamiltonian matrix of the outermost layers

(the principal layer) of the electrodes are the same as those of bulk electrodes.[16] For graphene electrodes, the size of the unit cell perpendicular to the transport direction should also be large enough so that the interaction between the central molecule and the periodic images can be negligibly small. Therefore, we increase the portions of the electrodes in the extended molecule region to examine the reliability of our models constructed in the text. Fig. S10 shows the optimized atomic structures of junctions with pyrazine anchors having longer or larger graphene electrodes than that of Junction-PG-V. As we can see, these newly constructed junction models have nearly the same transmission spectra as that of Junction-PG-V, especially for the transmission around $E_F$. Similar results are also obtained for junction models with the (5,5) armchair SWCNT electrodes (see Fig. S11), demonstrating that junction models reported in our manuscript can be reliably employed to describe the electronic transport properties of single-molecule junctions.

**Section 5:** Effects of the edge termination motifs of the graphene electrodes on the electronic transport properties of molecular junctions constructed with the pyrazine anchors
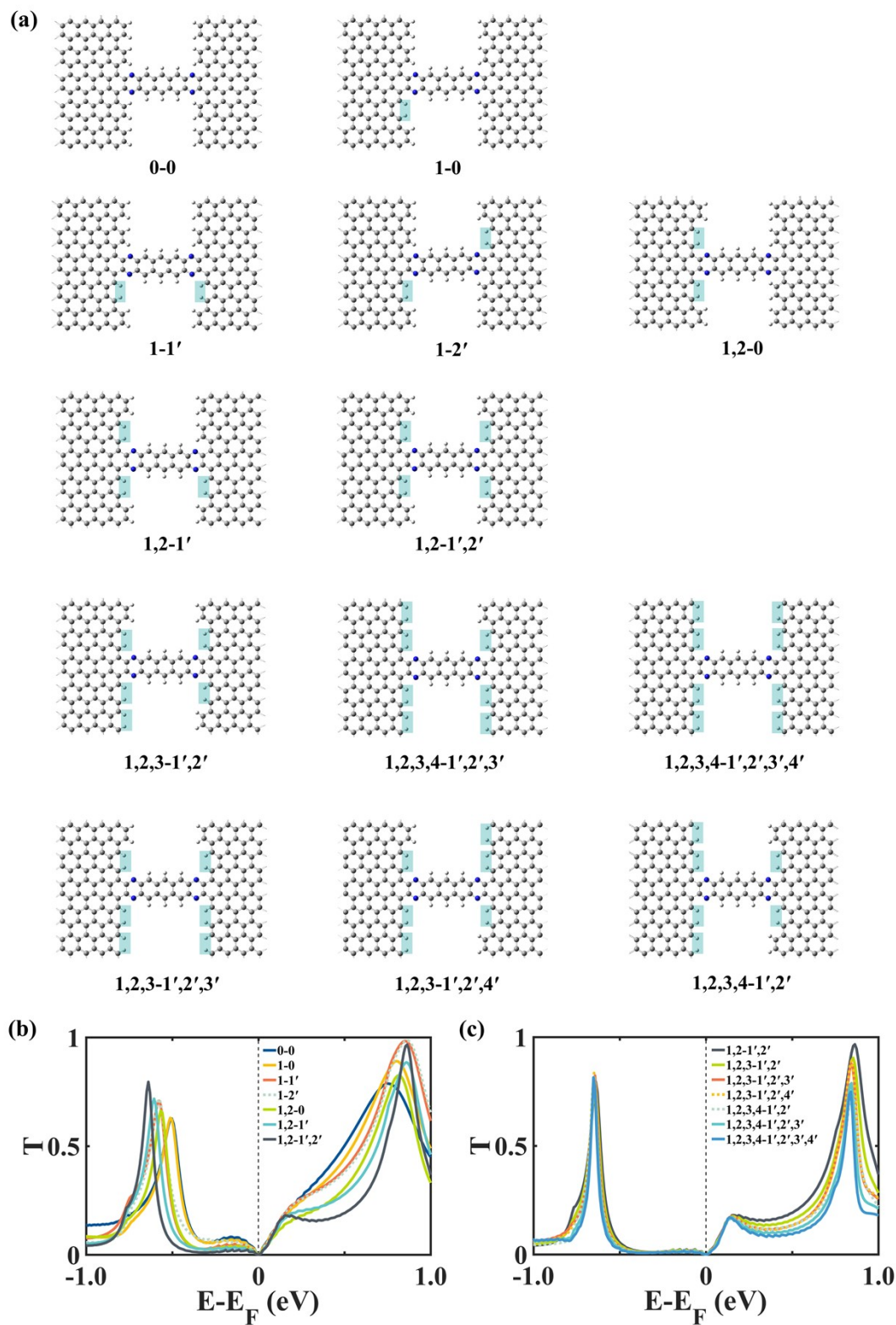
**(a)**



**(b)**          **(c)**



**Fig. S12** Optimized atomic structures (a) of molecular junctions with the consecutive removal of carbon dimers in the outmost first layer of the graphene electrodes and the corresponding equilibrium transmission spectra (b) and (c).
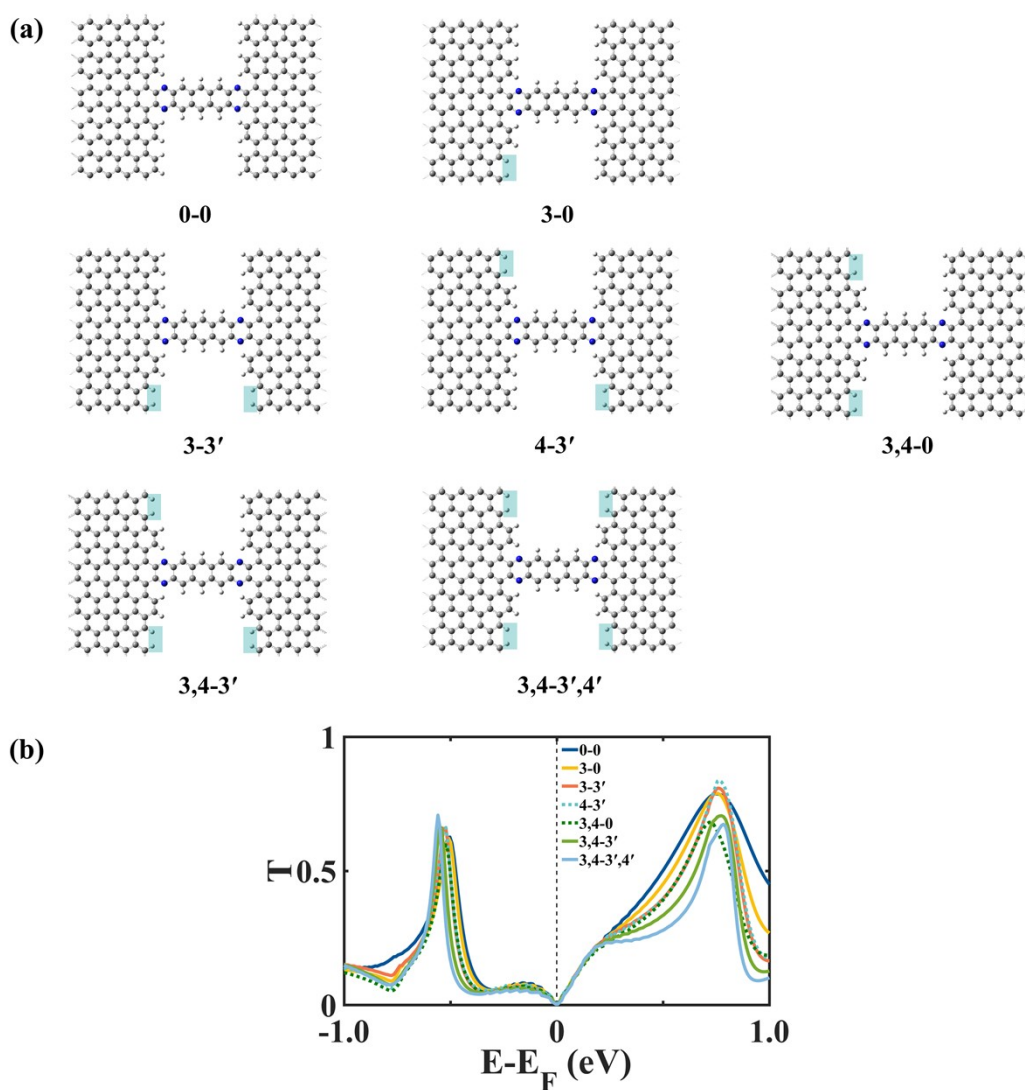
**Fig. S13** Optimized atomic structures (a) of molecular junctions with the removal of the carbon dimers away from the binding sites of M1 that are labelled 3, 4, 3′, and 4′, and the corresponding transmission spectra shown in (b).

In Fig. S12 the removal of carbon dimers in the outermost first layer of the graphene electrodes is started from those adjacent to the binding sites of the molecule M1 (denoted by 1, 1′, 2, and 2′) whereas in Fig. S13 similar operations are started from the carbon dimers away from the binding sites of the molecule M1 (denoted by 3, 3′, 4, and 4′). Clearly, the edge termination motifs of the graphene electrodes adjacent to the binding sites of the pyrazine anchors have a much larger influence on the junction transport.

**Section 6:** Effects of the diameter of armchair SWCNT electrodes on the electronic transport properties of molecular junctions constructed with pyrazine anchors
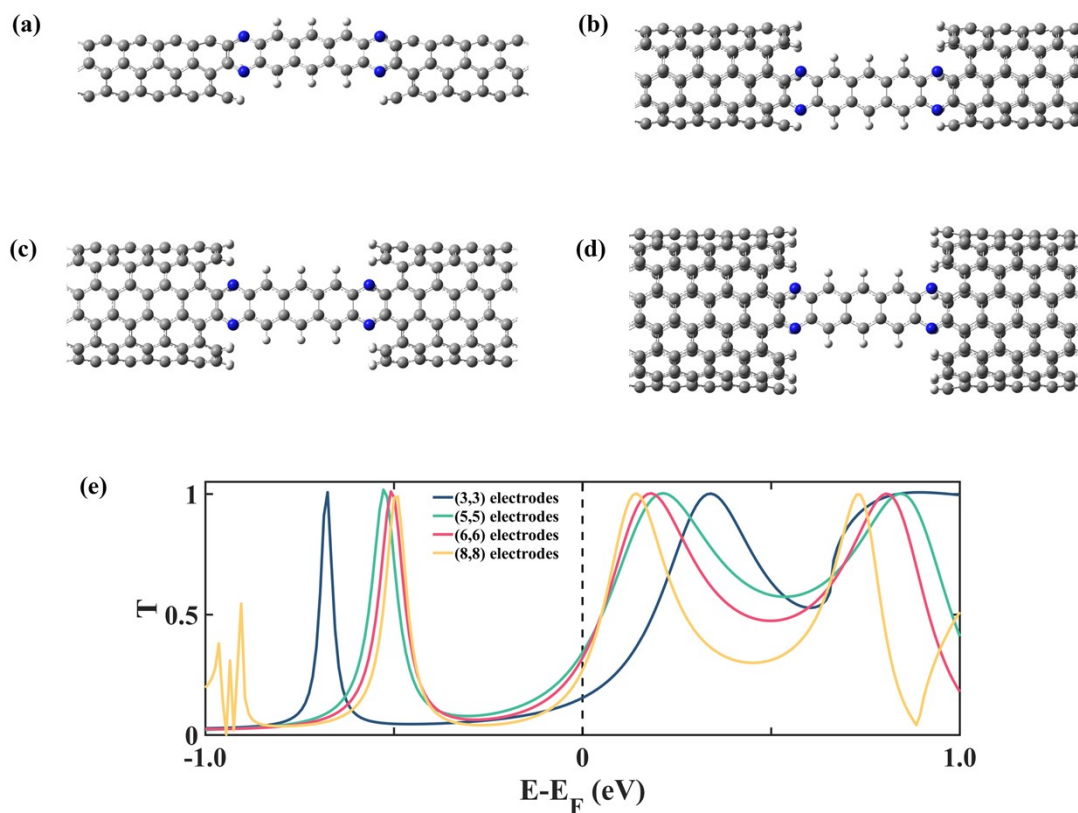


**Fig. S14** Optimized atomic structures of molecular junctions constructed with the pyrazine anchors and the (3,3) (a), (5,5) (b), (6,6) (c) and (8,8) (d) armchair SWCNT electrodes, and their corresponding equilibrium transmission spectra are shown in (e).

For molecular junctions constructed with the pyrazine anchors and the (5,5), (6,6) and (8,8) armchair SWCNT electrodes, the diameter of the SWCNT electrodes only has a minor influence on the energy positions and the heights of the HOMO- and LUMO-dominated transmission peaks so that the transmission around $E_F$ is almost the same. However, both the HOMO- and LUMO-dominated transmission peaks are shifted away from $E_F$ when the (3,3) armchair SWCNTs are used as the electrodes; correspondingly, the transmission coefficient at $E_F$ is changed to a lower value.

**Section 7:** Effects of the conformational flexibility of an anthracene molecule anchored with amide bonds on the junction conductance
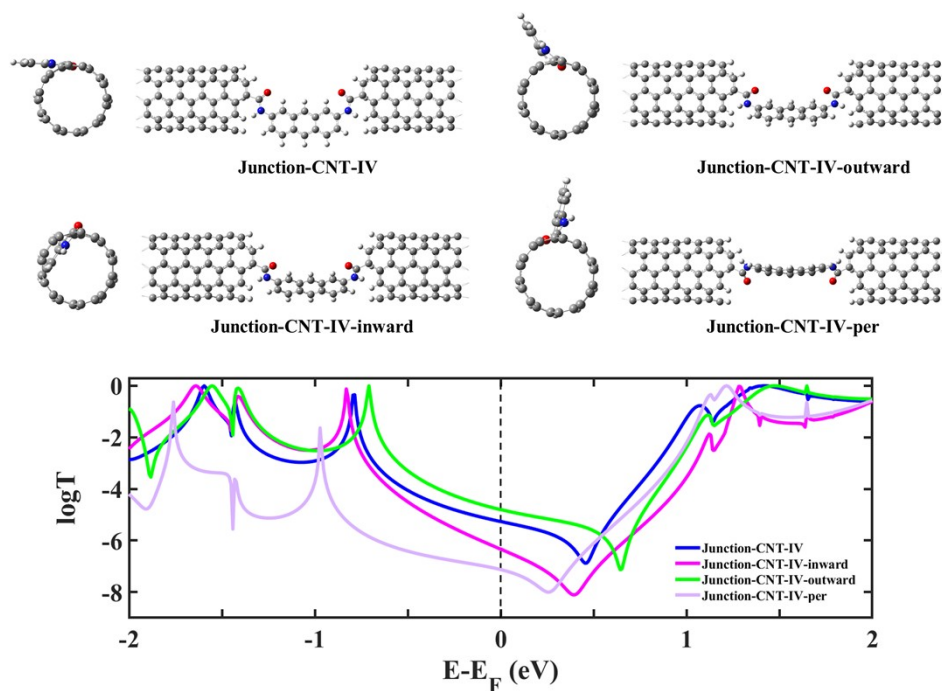


**Fig. S15** Optimized atomic structures of Junction-CNT-IV, Junction-CNT-IV-inward in which the anthracene molecule is rotated ~45° inward, Junction-CNT-IV-outward in which the anthracene molecule is rotated ~45° outward, and Junction-CNT-IV-per in which the anthracene molecule is rotated nearly perpendicular to the original molecular plane. Their corresponding equilibrium transmission spectra are also shown on a logarithmic scale. Note that all the junctions here are possible at room temperature due to their slight total energy differences.

As shown in Fig. S15, the anthracene molecule can adopt many configurations when it is sandwiched between the two semi-infinite (5,5) armchair SWCNT electrodes via amide anchors. Compared to Junction-CNT-IV, the anthracene molecule can be rotated ~45° inward and ~45° outward, even perpendicular to the original molecular plane. Correspondingly, the transmission coefficients at $E_F$ can vary by three orders of magnitude, indicating that the low-bias conductance of molecular junctions with amide anchors is very sensitive to the junction configurations. Consequently, more fluctuations will be observed in the conductance of molecular junctions with amide anchors, further demonstrating the super stability of the robust pyrazine anchors.

**Section 8:** Solvent effects of ethanol molecules on the low-bias conductance of molecular junctions constructed with pyrazine anchors and the (5,5) armchair SWCNT electrodes
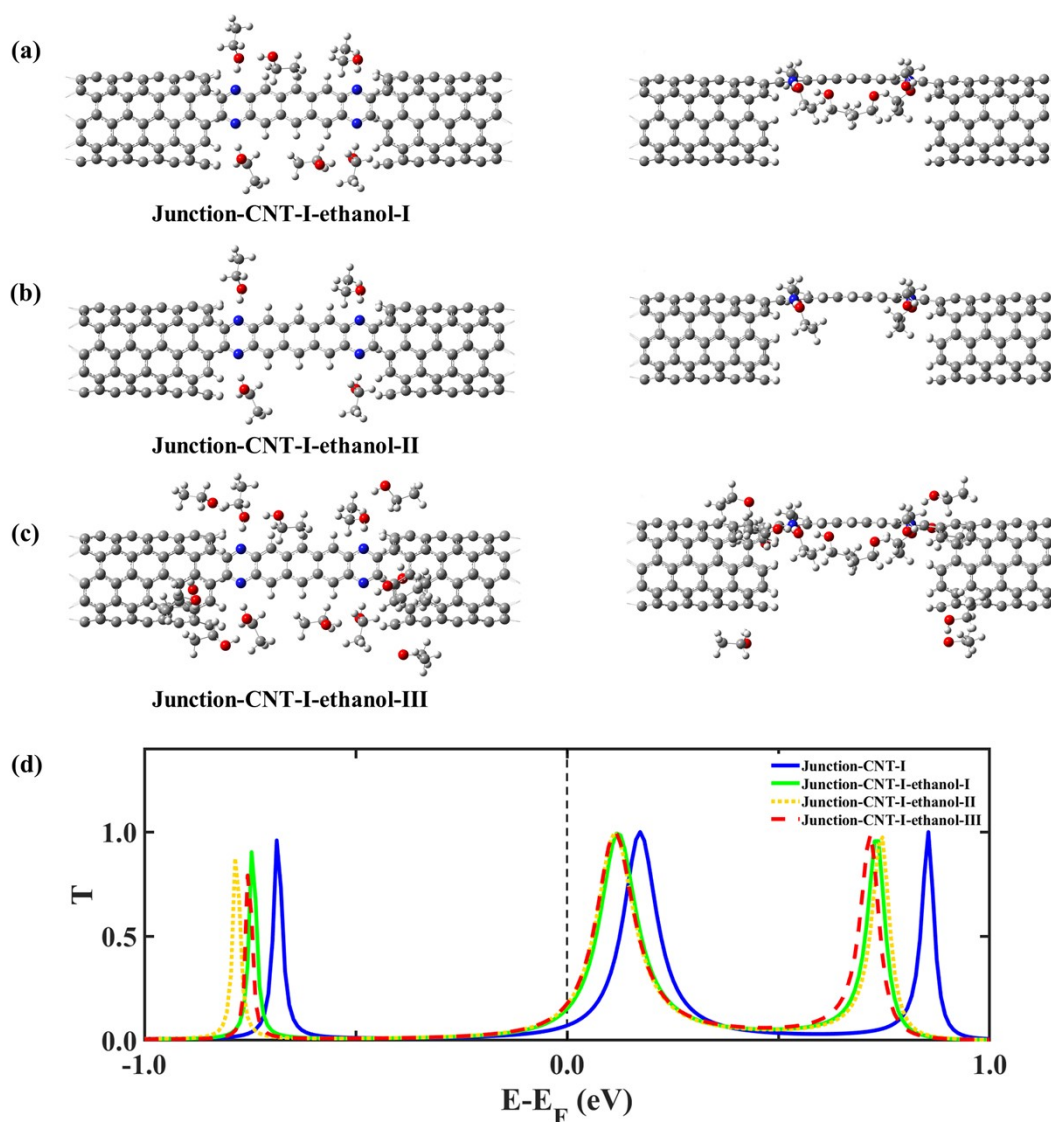


**Fig. S16** Top views and side views of the optimized atomic structures of Junction-CNT-I-ethanol-I (a) with six ethanol molecules added around the central molecule, Junction-CNT-I-ethanol-II (b) with only four ethanol molecules forming hydrogen-bond interactions with the pyridinic nitrogen atoms in the pyrazine linkages, and Junction-CNT-I-ethanol-III (c) with extra eight ethanol molecules added around the molecule-electrode interfaces. (d) Equilibrium transmission spectra for Junction-CNT-I-ethanol-I (solid green), Junction-CNT-I-ethanol-II (dotted yellow), and Junction-CNT-I-ethanol-III (dashed red). The equilibrium transmission spectrum for Junction-CNT-I is replotted in solid blue for comparison.

Taking Junction-CNT-I as an example, six ethanol molecules are now added around the central molecule M1 (see Fig. S16). After geometry optimization, four ethanol molecules form O-H⋯N hydrogen bonds with the four pyridinic nitrogen atoms in the pyrazine anchors, and the distances between the pyridinic nitrogen atoms and the nearest hydrogen atoms in the hydroxyl groups are in the range 1.85-1.92 Å; the other two ethanol molecule also form an O-H⋯O hydrogen bond with

their neighboring ethanol molecule. The introduction of these ethanol molecules shifts the transmission peaks to lower energies. For example, the LUMO-dominated transmission peak is shifted downward from 0.17 eV to 0.12 eV. As a result, the transmission coefficient at $E_F$ increases slightly from 0.07 to 0.14. Furthermore, when we add eight more ethanol molecules around the pyrazine-SWCNT interfaces or remove the two ethanol molecules that are not bonded directly to the central molecule M1, the obtained transmission spectra only change negligibly, suggesting that the solvent effects of the ethanol molecules are mainly caused by the hydrogen-bond interactions between the pyridinic nitrogen atom in the pyrazine linkages and the hydroxyl group in the ethanol molecules.

## References

1   T. Frederiksen, M. Paulsson, M. Brandbyge and A.-P. Jauho, *Phys. Rev. B*, 2007, **75**, 205413.

2   C. Bannwarth, E. Caldeweyher, S. Ehlert, A. Hansen, P. Pracht, J. Seibert, S. Spicher and S. Grimme, *WIREs Comput. Mol. Sci.*, 2021, **11**, e1493.

3   S. Spicher and S. Grimme, *Angew. Chem. Int. Ed.*, 2020, **59**, 15665-15673.

4   Gaussian 16, Revision A.03, M. J. Frisch, G. W. Trucks, H. B. Schlegel, G. E. Scuseria, M. A. Robb, J. R. Cheeseman, G. Scalmani, V. Barone, G. A. Petersson, H. Nakatsuji, X. Li, M. Caricato, A. V. Marenich, J. Bloino, B. G. Janesko, R. Gomperts, B. Mennucci, H. P. Hratchian, J. V. Ortiz, A. F. Izmaylov, J. L. Sonnenberg, D. Williams-Young, F. Ding, F. Lipparini, F. Egidi, J. Goings, B. Peng, A. Petrone, T. Henderson, D. Ranasinghe, V. G. Zakrzewski, J. Gao, N. Rega, G. Zheng, W. Liang, M. Hada, M. Ehara, K. Toyota, R. Fukuda, J. Hasegawa, M. Ishida, T. Nakajima, Y. Honda, O. Kitao, H. Nakai, T. Vreven, K. Throssell, J. A. Montgomery, Jr., J. E. Peralta, F. Ogliaro, M. J. Bearpark, J. J. Heyd, E. N. Brothers, K. N. Kudin, V. N. Staroverov, T. A. Keith, R. Kobayashi, J. Normand, K. Raghavachari, A. P. Rendell, J. C. Burant, S. S. Iyengar, J. Tomasi, M. Cossi, J. M. Millam, M. Klene, C. Adamo, R. Cammi, J. W. Ochterski, R. L. Martin, K. Morokuma, O. Farkas, J. B. Foresman, and D. J. Fox, Gaussian, Inc., Wallingford CT, 2016.

5   E. J. Baerends, O. V. Gritsenko and R. van Meer, *Phys. Chem. Chem. Phys.*, 2013, **15**, 16408-16425.

6   E. J. Baerends, *Phys. Chem. Chem. Phys.*, 2017, **19**, 15639-15656.

7   J. Heyd, G. E. Scuseria and M. Ernzerhof, *J. Chem. Phys.*, 2003, **118**, 8207-8215.

8   J. Heyd and G. E. Scuseria, *J. Chem. Phys.*, 2004, **120**, 7274-7280.

9   J. Heyd and G. E. Scuseria, *J. Chem. Phys.*, 2004, **121**, 1187-1192.

10  J. Heyd, G. E. Scuseria and M. Ernzerhof, *J. Chem. Phys.*, 2006, **124**, 219906.

11  J. Tao, J. P. Perdew, V. N. Staroverov and G. E. Scuseria, *Phys. Rev. Lett.*, 2003, **91**, 146401.

12  S. Datta, *Quantum Transport: Atom to Transistor,* Cambridge University Press, Cambridge, 2005.

13  J. Hafner, *J. Comput. Chem.*, 2008, **29**, 2044-2078.

14  G. Kresse and J. Furthmüller, *Phys. Rev. B*, 1996, **54**, 11169-11186.

15  G. Kresse and D. Joubert, *Phys. Rev. B*, 1999, **59**, 1758-1775.

16  A. R. Rocha, V. M. García-Suárez, S. Bailey, C. Lambert, J. Ferrer and S. Sanvito, *Phys. Rev. B*, 2006, **73**, 085414.